Size and strain dependent activity of Ni nano and micro particles for hydrogen evolution reaction

Alexandra Pătru [a], Philippe Antitomaso [a], Remy Sellin [a], Nicolas Jerez [b], Pierre Louis Taberna [c], Frédéric Favier [a,*]

[a] Institut Charles Gerhardt Montpellier, ICGM, UMR 5253 CNRS, Université Montpellier 2, cc1502, 34095 Montpellier cedex 05, France
[b] Bulane SAS, 15 Rue Paul Doumer, 34690 Fabrègues, France
[c] CIRIMAT, UMR 5085 CNRS, Université Paul Sabatier, 31062 Toulouse, France

ARTICLE INFO

Keywords:
Hydrogen evolution
Alkaline water electrolysis
Nickel nanoparticles
Electrochemical
impedance spectroscopy

ABSTRACT

In the context of constant research for the improvement of alkaline water electrolysis process using advanced electrocatalytic materials for the hydrogen evolution reaction (HER), various nickel particle based electrode materials were prepared and characterized. The synthesis of nickel hydroxide nanoparticles was performed in water in presence of three different stabilizers (CTAB, PVP and KBr). A thermal treatment at 400 °C under 5% H_2/Ar atmosphere led to nickel nanoparticles. Mechanically milled commercial micrometric particles and nanoparticles synthesised by a polyol route completed a series of Ni powders showing broad ranges of size (5 nm 73 μm) and strain (6 ppm 0.7%). The electrocatalytic activity of the resulting electrode materials was evaluated versus powder morphology. Their apparent and intrinsic activity and the mechanism of the HER were studied by electrochemical impedance spectroscopy (EIS) and steady state polarisation. A change in the HER mechanism is observed depending on particle size. This first systematic study demonstrates that the smaller the size and the more defective the particles, the greater the electrocatalytic activity. As a matter of fact, appreciable cathodic current densities of 100 mA cm ^{2} at ~ 300 mV of overpotential were obtained for nickel nanoparticles with 5 nm size and 0.7% strain.

1. Introduction

Nowadays, hydrogen is considered as a promising energy carrier and alternative to fossil fuels. Alkaline water electrol ysis is one of the easiest methods for pure hydrogen produc tion, offering the advantage of simplicity. The challenges for the widespread use of water electrolysis are to reduce asso ciated energy consumption, cost and maintenance and to in crease reliability, durability and safety of the systems [1].

Besides raw material cost, the energy consumption and associated cost are currently too high [2]. These are directly proportional to the operational cell voltage which depends on the overpotential for the cathodic and anodic reactions and on the internal resistance in the cell. The cost of hydrogen pro duction by water electrolysis can thus be drastically reduced by decreasing the overpotential of the electrode reactions as well as by selecting inexpensive electrode materials. There are two critical parameters for overpotential decrease, one is

* Corresponding author. Tel.: +33 46 714 33 32.
E mail address: fredf@univ montp2.fr (F. Favier).
http://dx.doi.org/10.1016/j.ijhydene.2013.06.045

geometric and a second is electronic. The former depends on the surface area developed by the electrode material at which the reaction is taking place. The latter depends on the nature of the material used and on its intrinsic activity.

Nickel is a good candidate for hydrogen evolution reaction (HER). It combines satisfactory electrocatalytical activity and chemical stability in alkaline solutions, and it is cheaper than platinum, the reference catalyst for this reaction. However, to improve its activity, i.e. decrease the overpotential for the HER, the developed surface area should be increased. This can be achieved by using Ni in the form of nanoparticles and, since HER is a highly surface sensitive reaction, nanoparticles should show optimised surface morphologies.

Many papers have reported the use of nickel –based electrodes with high surface area for HER. On one hand, an increase in the developed surface area can be achieved through several methods including the deposition of nickel together with a secondary active material such as Al and Zn by pressing [3,4], electrodeposition [5] or thermal spray [6], followed by the dissolution of the secondary component (Raney types electrodes), but also high current density elec trodeposition of nickel [7] [8], or electrodeposition of nickel on silica or polystyrene opals followed by a selective removal of the opals [9]. On the other hand, increased intrinsic ac tivity has been achieved by alloying Ni with some metals: NiCo [10,11], NiMo [12–15], $NiMoO_x$ [16], NiFe [17], NiMn [18], NiCu [19], Ni Rare earth [20]. Only a limited number of papers discusses the HER on pure nickel nanoparticles [21,22] and nanowires [23].

The aim of this work is to explore the HER mechanism and to find the optimal design of the electrode material for this reaction using nickel nanoparticles showing various mor phologies, sizes and strain.

In the first part of this paper, a new aqueous route is pro posed for nickel nanoparticle synthesis. The nickel nano particles obtained by this approach were compared with nanoparticles obtained by a polyol route and with commercial nickel particles, as purchased or mechanically milled. The resulting morphologies were characterized by electron mi croscopies and X ray diffraction. In the second part, electro chemical measurements were routinely performed by cyclic voltammetry, steady–state polarisation and AC impedance techniques to evaluate the impact of the Ni powder morphology on the electrode performances.

2. Experimental method

2.1. Materials

Chemicals and reagents were used as received. $NiCl_2$. $6H_2O$ (99.9998% Puratronic®) was purchased from Alfa Aesar. Hex adecyltrimethylammonium bromide (CTAB 99%), sodium borohydride $NaBH_4$ (≥96%), polyvinylpyrrolidone with average molecular weight 1 200 000 g/mol (PVP 1200), potassium hy droxide (99.99%) and nickel powder (5 μm, 99.7%) were pur chased from Sigma Aldrich. Ammonia solution 28% was purchased from VWR. Potassium bromide was purchased from Merck. Deionized water with 18.2 MΩ cm resistivity was obtained from a Milli Q water purification system and used for the preparation of all the solutions. 99% purity Ni foils were purchased from Goodfellow. Stainless steal 316 L grids were purchased from Gantois.

2.2. Synthesis of nickel nanoparticles

2.2.1. Synthesis in aqueous medium

A calculated amount of $NiCl_2$. $6H_2O$ solution, used as Ni^{2+} precursor, was added dropwise to a 50 mL NH_3 aqueous so lution, under magnetic stirring (200 rpm). The temperature was kept constant at 25 °C with the help of a thermo regulated water bath.

The mixture was prepared so to end up with 0.01 M $NiCl_2$. $6H_2O$ and 0.03 M NH_3 respective concentrations. After 15 min, a stabilizing agent was added. Three different stabilizing agents were used: CTAB, PVP and KBr. At this step, two different pathways could be followed:

Pathway #1 the synthesis was stopped after the addition of the stabilizing agent.

Pathway #2 a 0.5 M solution of $NaBH_4$ was added using a peristaltic pump to the mixture at a rate of 0.1 mL min^{-1}.

Hydroxide nanoparticles were obtained through both synthetic pathways.

The hydroxide nanoparticles synthesized using PVP as stabilizers were separated from solution by centrifugation (4000 rpm, 90 min). Nanoparticles synthesized using the other stabilizing agents were filtrated on Buchner, washed using a water–acetone mixture, until the disappearance of chloride and finally dried under vacuum. The synthesized materials were annealed for 3 h at 400 °C under Ar–5%H_2 with a 1 °C min^{-1} heating ramp. To determine the optimal annealing temperature, an *in situ* X ray diffraction (XRD) study was performed. The corresponding XRD results are given in the SI section, Fig. SI 1.

2.2.2. Synthesis in ethylene glycol

Ni particles were synthesized by the so called polyol route as described elsewhere [24]. Briefly, a 0.01 M $NiCl_2$. $6H_2O$ solution in ethylene glycol was heated to 140 °C in a 100 ml three neck round bottom flask equipped with a condenser. At this tem perature, 0.36 g $NaBH_4$ powder was added under strong mag netic stirring, immediately leading to the formation of a black precipitate. No stabilizing agent was used. The solid was separated by filtration, washed and dried in the same manner as described in section 2.2.1.

2.3. Mechanical milling

A commercial nickel powder was used as starting material for mechanical milling. The powder was introduced under nitrogen atmosphere into a stainless steel container with stainless steel balls. The milling was performed in a planetary mill (Retsch PM 100) with a rotation speed of 400 rpm and different milling times: 10 min, 1, 3 and 12 h respectively.

2.4. Physical and physicochemical characterizations

The structures of the synthesized nickel nanoparticles and of the milled Ni powders were characterized by XRD using an

X'Pert Philips diffractometer operated with Cu Kα radiation. The diffraction patterns were analyzed using the Maud 3.22 software.

Size strain broadening was evaluated through equation (1) as, the instrumental XRD broadening determined from a LaB_6 standard sample was subtracted from the total broadening

$$B\cos\theta \quad \frac{0.9\lambda}{d} + e\sin\theta \qquad (1)$$

d, as the grain diameter, and e, as the lattice strain, can be calculated with B as measured width at half maximum intensity of the considered diffraction peak at θ Bragg angle and λ as the X ray wavelength (CuKα).

Surface morphologies of chemically synthesized nickel nanoparticles were examined using transmission electron microscopy (TEM) (JEOL – 1200EX – 2). The milled nickel particles were imaged using scan electron microscopy (SEM) (FEI Quanta FEG 200). For each sample, corresponding mean particle sizes and size distributions were measured for 200 isolated particles.

2.5. *Electrochemical measurements*

The electrochemical measurements were carried out in a standard three electrode electrochemical cell. A platinum foil of 4 cm^2 was used as counter electrode and a Ag/AgCl in 3 M NaCl (M2 Materials Mates, type R4/AGCL/S7) as reference electrode. The latter was connected through a Luggin capillary to the working electrode compartment. A solution of 1 M KOH in ultrapure water was used as electrolyte. The voltage–current density curves as well as electrochemical impedance spectroscopy (EIS) were recorded using a high power potentiostat (BioLogic VMP3). Before each experiment, the electrolyte was purged by bubbling nitrogen (U quality) for 30 min. The nitrogen atmosphere was maintained in the electrochemical cell during measurements. Electrodes were prepared in the form of films deposited on a stainless steel grid with 5 mg cm^{-2} nickel loading.

All electrochemical measurements were done at 20 °C. Cyclic voltammograms were recorded from oxygen (anodic range) to hydrogen (cathodic range) evolution potentials at a scan rate of 50 mV/s. Polarization curves were recorded at 1 mV/s scan rate from 0.95 to 1.7 V/Ref. The second scan was used for analysis. Before polarisation measurement, the working electrode was kept at 1.2V/Ref for 15 min in the electrolyte solution to reduce the native oxide film at the electrode surface. The metallic nature of the electrode surface was confirmed by running a CV right after such a polarization step (see Fig. SI 2). Curves were corrected for ohmic drop effect. The series resistance was previously determined from EIS measurements. Impedance spectra were recorded in the frequency range of 1 MHz–10 mHz in potentiostatic mode at four different potentials corresponding to moderate HER overpotentials (0.025, 0.075, 0.125, 0.175 V). The voltage amplitude was 10 mV. The experimental data were fitted to the equivalent electrical circuits by a randomize simplex procedure using Zfit EC Lab software.

3. Results and discussions

3.1. *Structural characterization*

Particle composition and crystallinity were evaluated for each prepared powders. For nickel nanoparticles synthesized in water medium, the first focus was on the effect of $NaBH_4$ addition. With or without $NaBH_4$ addition, nickel hydroxide nanoparticles were produced as confirmed by the XRD patterns shown in Fig. 1. $NaBH_4$ was expected to reduce either the hydroxide or, before hydroxide formation, solubilised Ni^{2+} as Ni metal. Despite a colour change from green to black of the suspension upon addition of $NaBH_4$, nickel hydroxide was detected by XRD in both cases (Fig. 1). The main reaction step sequences proposed for these two processes are represented in Fig. 2.

For pathway#2, the reaction is suggested to proceed by reduction by $NaBH_4$ of hexagonal, well crystallized nickel hydroxide particles through a solid–liquid mechanism to promote the growth of small nickel particles (see insert Fig. 3B). Because of the mild pH aqueous environment, these nickel particles are quickly hydroxilated back. Through this method, nickel hydroxide nanoparticles with various morphologies are obtained (Fig. 3). A thermal treatment under reductive atmosphere (5%H_2/Ar) is necessary to obtain metallic nickel nanoparticles.

Fig. 4A shows the XRD patterns in the series of as synthesized nickel nanoparticles. The diffraction peaks correspond to cubic Ni metal (PDF card no.00 001 1260).

From the broadening of the XRD peaks both average crystallite sizes and lattice stains were calculated. Corresponding values are summarized in Table 1.

Obviously, the calculated average grain size and strain depend on the synthesis route and stabilizing agent. Nanoparticles obtained by $NaBH_4$ reaction are smaller than without $NaBH_4$. Depending on the nature of the stabilizing agent used, particle sizes range from 15 nm (CTAB, surfactant effect) to 42 nm (KBr, halogen stabilizing effect). Nickel crystallites

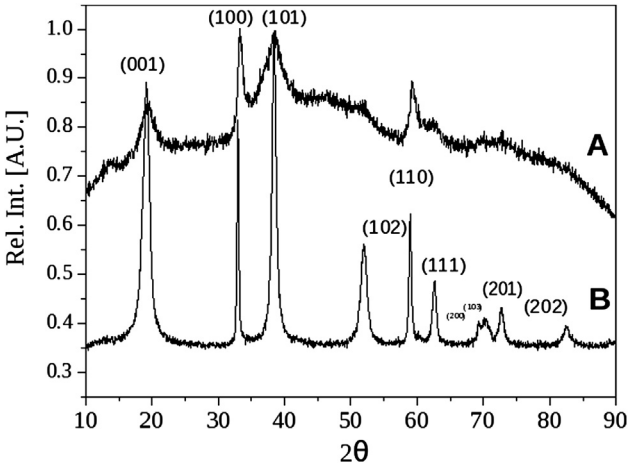

Fig. 1 – The X-ray diffraction of prepared $Ni(OH)_2$ nanoparticles with $NaBH_4$ (A) and without $NaBH_4$ (B).

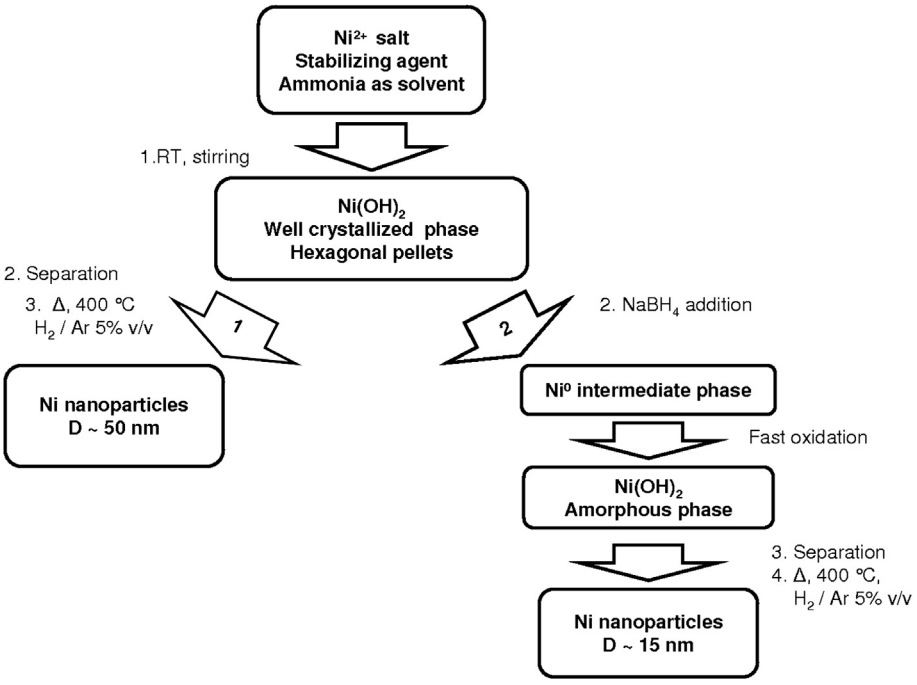

Fig. 2 – Reaction step sequence proposed for the two different synthesis pathways.

synthesized in ethylene glycol are smaller than those synthesized in aqueous medium. As such, the thermal treatment needed in case of the aqueous route, is suspected to promote the growth and aggregation of nanoparticles.

On the other hand, the observed lattice strains are greater for nickel particles synthesized by the polyol route than for those by aqueous synthesis. This can also be explained by the strain release occurring during the reducing thermal treatment of prepared nickel hydroxide particles. A reduction under hydrogen atmosphere and high temperature is known to facilitate the formation of large crystallites by reducing the activation energy of migration of defects, generally through mobile hydride formation [25].

To expand the set of nickel particle morphologies and sizes, nickel particles were also obtained by milling a commercial Ni powder. The XRD patterns evolution with the milling time is shown in Fig. 4B. By increasing the milling time, the position of the (111) reflexion peak shifts to lower diffraction angles and the peak widths tend to broaden. After a 12 h ball milling step duration, the grain size decreased from 178 nm to 26 nm as the lattice strain increased from 0.093 to 0.235%. XRD results obtained for all these samples are shown in Table 1 and Fig. SI 3.

In electrochemical systems, the size measured by electron microscopy is considered as more physically consistent than the crystallite size extracted from XRD measurements because of the close relation between accessible surface and geometrical surface deduced from electron microscopy. The TEM images of the various samples synthesized in aqueous environment are shown in Fig. 5. Fig. 5A′, B′, C′ and D′ presents the corresponding size frequency histograms. The sample synthesized without $NaBH_4$ shows quasi spherical particles,

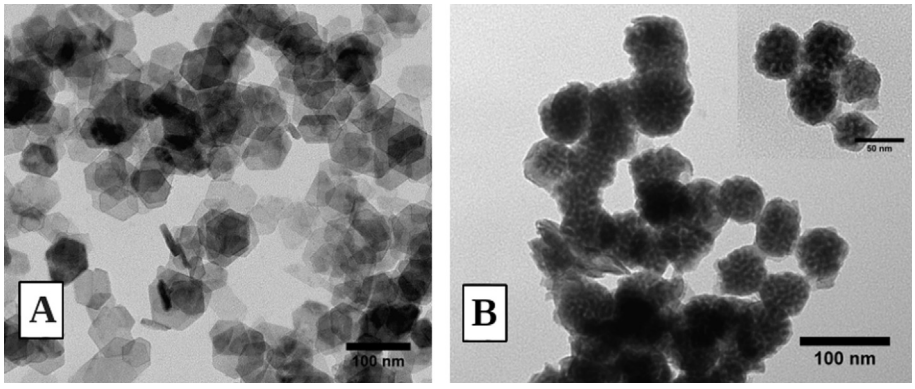

Fig. 3 – TEM images of (A) $Ni(OH)_2$, (B) $Ni(OH)_2$ prepared without or by addition of $NaBH_4$ respectively. In both cases, CTAB is used as stabilizer.

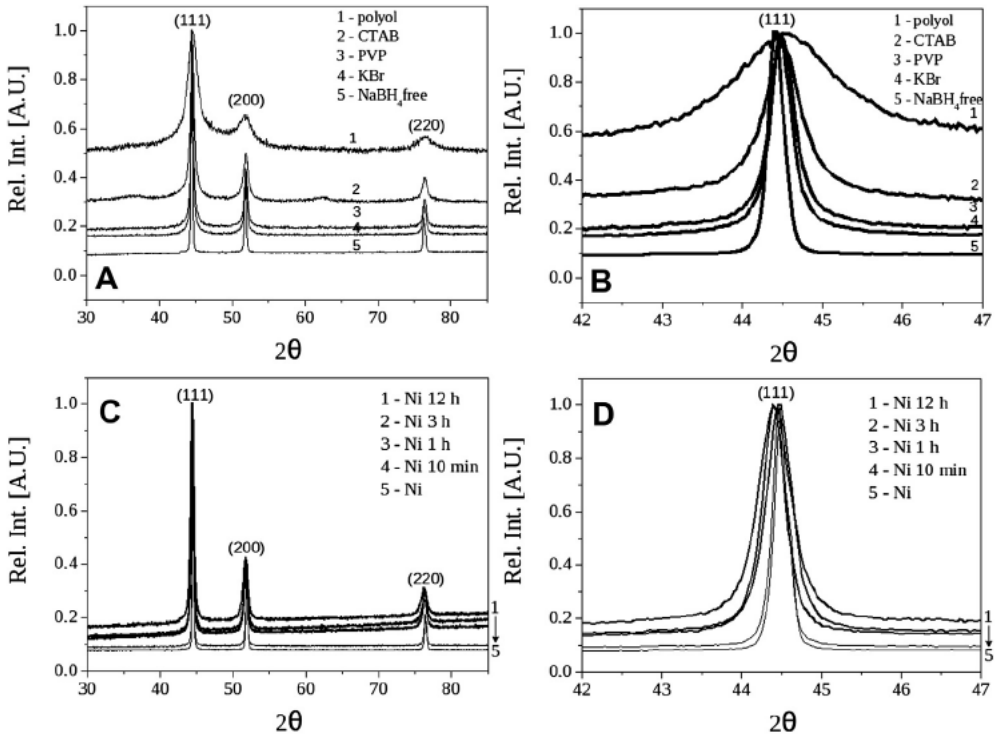

Fig. 4 – XRD patterns of the chemically synthesised nickel nanoparticles (A) and milled nickel micro-particles (C). (B) is a zoom-in of the (111) peak range corresponding to (A) and (D), a zoom-in of the (111) peak range corresponding to (C).

with a roughly Gaussian particle size distribution. The average particle size is 52 nm (Fig. 5A et A′).

Particles synthesized by using $NaBH_4$ and various stabi lizing agents exhibit spherical shapes and are isolated or moderately aggregated particles (Fig. 5B, C, D). In each case, particle size distribution can be fitted with a log normal distribution (Fig. 5B′, C′, D′). The average sizes extracted from the size distribution of these samples are reported in Table 1.

Fig. 6 shows the evolution of the morphology as observed by SEM of the powder milled for various durations. Morphol ogies are greatly affected by the mechanical milling duration. The characteristic average particle and crystallite sizes ob tained by SEM and XRD respectively are reported in Table 1.

After a milling period of 3 h, particle sizes measured by SEM increased from 1.15 to 73 μm, by prolonging the milling time up to 12 h, particle size decreased to 38 μm. This observation is in good accordance with the two well known processes, cold welding and fracture, already described for materials prepared by mechanical milling [26]. Zhao et al. observed a similar behaviour for nickel particles prepared by mechanical milling [27]. They found that below 10 h of milling the dominant stage is cold welding while after 10 h, fracture is favoured.

Table 1 – Morphological and microstructure parameters extracted from XRD, SEM and TEM characterizations of synthesized nickel powders. L_v as the coherence domain average size (crystallite average size) and e as average strain parameter are estimated by using equation (1).

Sample chemical syntheses	XRD		TEM/SEM
	Lv, nm	Strain $e^{*}10^{3}$	Mean size, nm
Ni CTAB	15	0.05	11
Ni KBr	42	0.006	22
Ni PVP	35	1.2	27
Ni $NaBH_4$ free	126	0.04	52
Ni polyol	8	7.3	5
Mechanical syntheses	Lv, nm	Strain $e^{*}10^{3}$	Mean Size, μm
Ni commercial	178	0.93	1.15
Ni 10 min	113	0.99	1.8
Ni 1 h	38	1.6	37
Ni 3 h	34	1.7	73
Ni 12 h	26	2.35	38

3.2. *Voltammetric behaviour of nickel nanoparticles electrodes*

By immersion into KOH solution at open circuit potential, a layer of nickel hydroxide, α $Ni(OH)_2$ is spontaneously formed at the nickel surface [28]. With ageing (especially in concen trated alkali solution), α $Ni(OH)_2$ can dehydrate and recrys tallize as an anhydrous phase, β $Ni(OH)_2$ [29]. The oxidation peak corresponding to the formation of the nickel hydroxide layer can be observed if the first scan is performed quickly after the immersion of the nickel electrode in the KOH solu tion and after cathodic polarisation measurements. This peak starts at potentials below 1 V/Ref (see for example Fig. SI 2).

The anodic peak starting at 322 mV/Ref and its corresponding reduction peak is assigned to the transformation of Ni (II) species (hydroxides) in Ni (III) species (oxyhydroxides). A major advance in the understanding of Ni (II) → Ni (III) transition was made by Bode et al. [30]. They described the behavior of nickel hydroxide films by considering two distinct phases: α $Ni(OH)_2 + OH$ γ $NiOOH + e + H_2O$, and β $Ni(OH)_2 + OH$ β $NiOOH + e + H_2O$.

The oxidation of α $Ni(OH)_2$ to γ NiOOH is shown to occur at a lower potential than the redox transition between the two β phases. Moreover, the reduction of the oxyhydroxides (γ and β) gives rise to two distinct reductions peaks. The composition of the oxide film at a given potential depends on a wide range of factors including its chemical history, the preparation method of nickel particles preparation, concentration of defects, degree of hydration, etc.

Fig. 7 shows the fifth cycle of the cyclic voltammograms of nickel particle based electrodes measured in 1 M KOH aqueous solution at a sweep rate of 50 mV/s. In the whole series, oxidation and reduction peaks are unambiguously observed with the exception of the CTAB stabilized nickel nanoparticles. Intensities of the oxidation and reduction peaks are proportional with the surface in contact with the electrolyte. These intensities are well correlated with the particle sizes

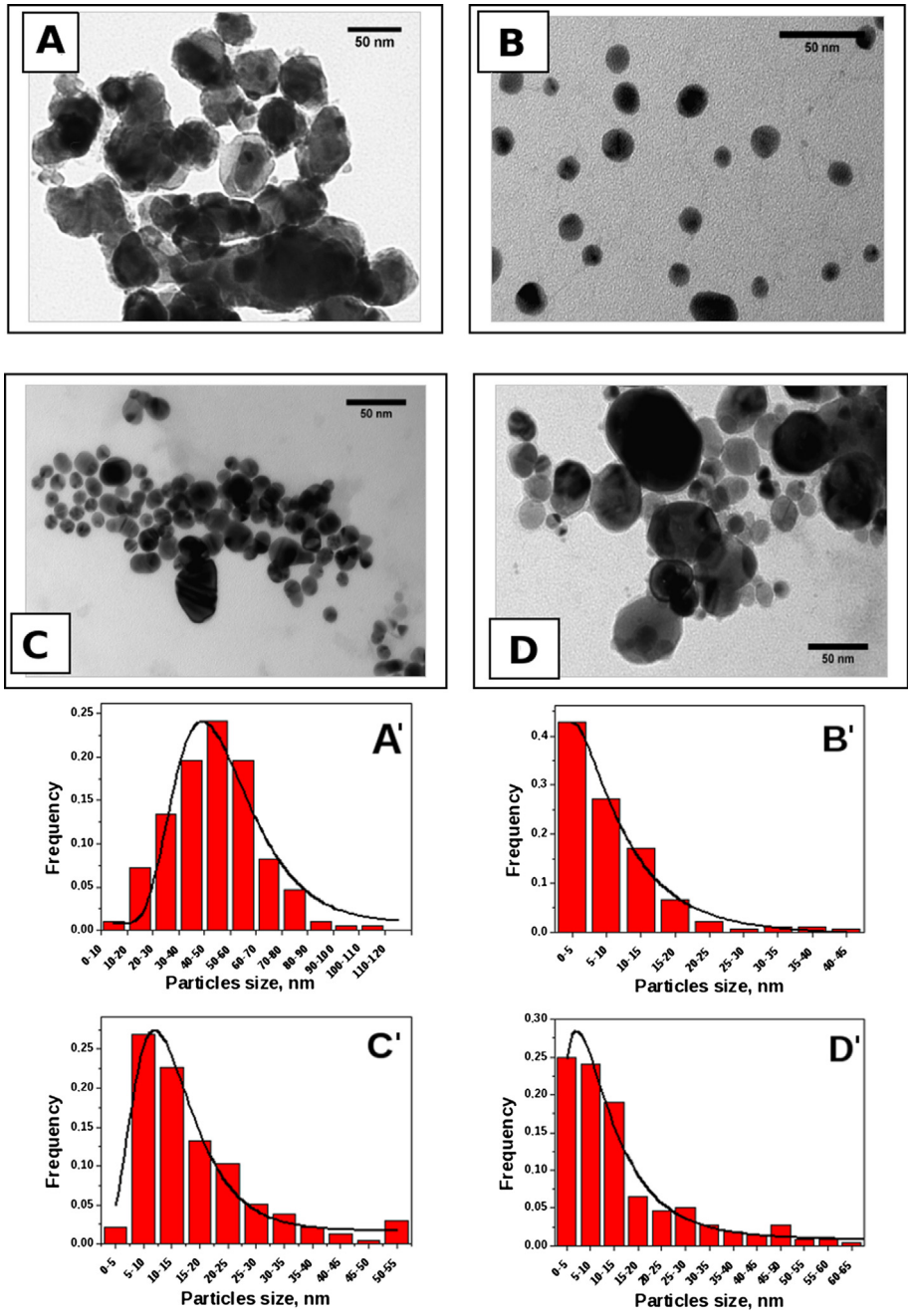

Fig. 5 – TEM images of Ni nanoparticles prepared without $NaBH_4$ (A), with CTAB (B), with PVP (C), with KBr (D) and the corresponding size histograms (A′), (B′), (C′), and (D′).

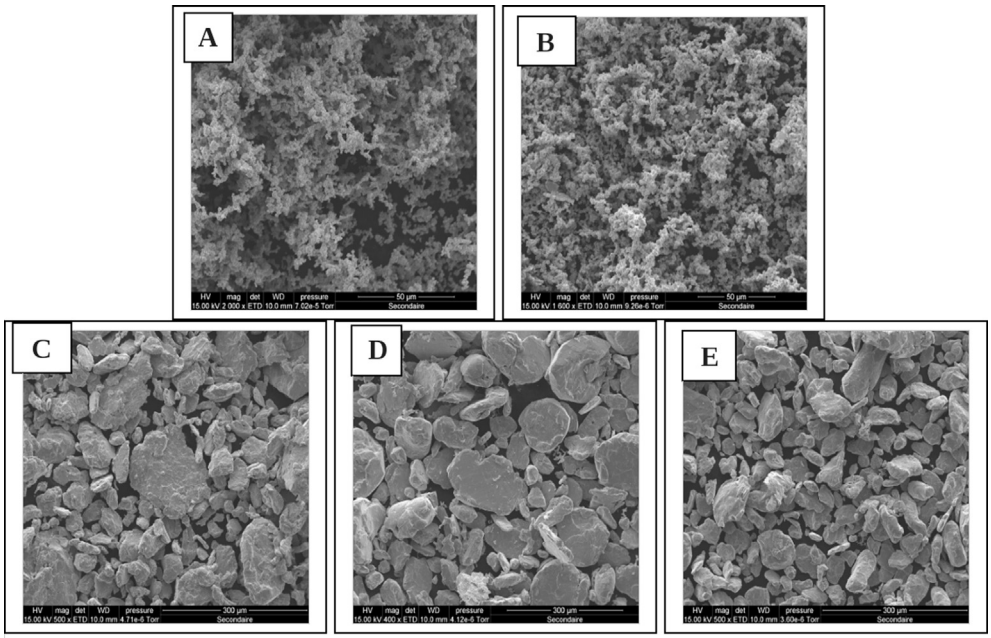

Fig. 6 – SEM micrographs of the milled nickel powders: (A) non-milled, (B) milled for 10 min, (C) milled for 1 h, (D) milled for 3 h, (E) milled for 12 h.

estimated by TEM in accordance with the corresponding developed surface area.

For particles with an average size larger than 52 nm, the oxidation peak is well defined whereas this peak is nearly absent for smaller particles. In the latter case, this can be explained by the overlap of this peak with the beginning of the oxygen evolution reaction. The cyclic voltammograms from the nanoparticles stabilized with CTAB significantly differe from those obtained for other particles. This difference is assigned to a phase heterogeneity including some nickel (II) oxide traces, NiO, as revealed by XRD (Fig. 4). Side reactions with CTAB during the reduction process under hydrogenated argon probably originate for the formation of this nickel oxide. This powder will not further be included in the present study for discussion about HER.

3.3. *Hydrogen evolution*

3.3.1. *Cathodic polarization curves*

To investigate the electrocatalytic activity of synthesized par ticles, kinetics parameters were derived from Tafel linear po larization measurements. Curves from a commercial smooth nickel foil electrode were also included for comparison.

For the linear part of the steady state polarization curve, the kinetics equation can be written as in Equation (2).

$$\eta \quad \frac{2.303RT}{\beta zF}\log j_0 \quad \frac{2.303RT}{\beta zF}\log j \quad a + b\log|j| \tag{2}$$

The characteristic parameters, the Tafel slope, b and ex change current density, j_0, were calculated using Equation (2). The Tafel slope b is characteristic of the mechanism for the

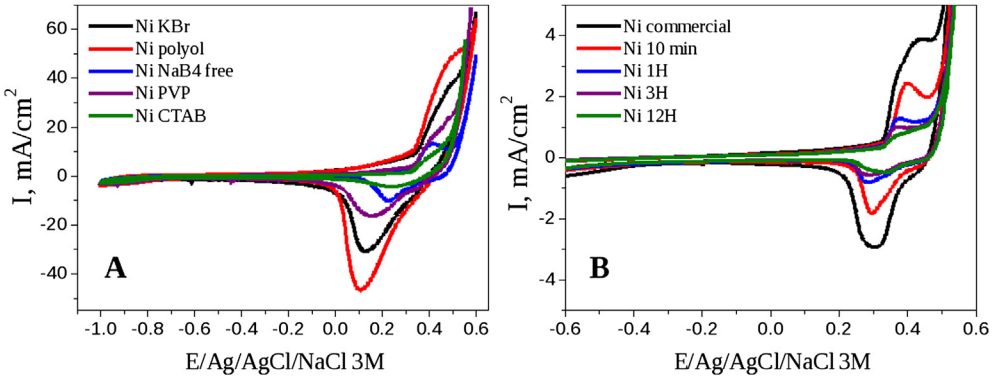

Fig. 7 – 5th cycle of cyclic voltammetric curves of the Ni nanoparticles based electrodes obtained by chemical synthesis (A) and by mechanical milling (B). CVs were recorded with a sweep rate of 50 mV/s.

HER, and the apparent current exchange density j_0, provides information on the intrinsic catalytic activity of the electrode material. Moreover, the apparent activity of the various electrodes was measured for a given overpotential η_{100} corresponding to a current density of 100 mA/cm^2.

The mechanism of HER in alkaline aqueous solutions involves the formation of an adsorbed hydrogen intermediate, MH_{ads} (Volmer reaction, eq. (3)), the electrodesorption of hydrogen (Heyrovsky reaction, eq. (4)) and/or a chemical desorption by the combination of two adjacent adatoms (Tafel reaction, eq. (5))

$$H_2O + M + e \Leftrightarrow MH_{ads} + OH \quad (3)$$

$$H_2O + MH_{ads} + e \Leftrightarrow H_2 + M + OH \quad (4)$$

$$2MH_{ads} \Leftrightarrow H_2 + 2M \quad (5)$$

Where M is a free site on the metal surface and MH_{ads} is a metal surface site occupied by an adsorbed hydrogen adatom. According to this general model for HER mechanism in alkaline medium, three distinct Tafel slopes can be calculated, depending on the limiting step (3), (4) or (5).

If the Volmer reaction, step (3), i.e. the disruptive adsorption of a water molecule, is the rate limiting step, the corresponding Tafel curve slope is theoretically 116 mVdec^{-1} at 20 °C. If the electrochemical desorption (4), i.e. Heyrovsky step, is rate limiting, the corresponding Tafel slope is expected above 38 mVdec^{-1}. If the chemical desorption step of hydrogen (5) is rate limiting, a theoretical slope of 29 mV dec^{-1} is expected.

Fig. 8 shows two sets of Tafel curves measured at 20 °C on the chemically synthesized nickel nanoparticles (A) and on the mechanically milled nickel particles (B). The values of the kinetics parameters extracted from these data are reported in Table 2. As shown in Fig. 8A, the polarization curves obtained for the chemically synthesized nickel nanoparticles are characterized by two Tafel slopes, at lower overpotential (LO) between 38 and 110 mV dec^{-1} and at high overpotential between 221 and 132 mV dec^{-1}. The polarization curves measured for nickel particles prepared by mechanical milling are characterized by a single Tafel slope ranging from 102 to 129 mV dec^{-1}.

From data reported in Table 2, a correlation between the Tafel slope and the particle structural characteristics can be drawn. Small particles, corresponding to the largest developed surfaces, give polarization curves with two Tafel slopes. As the particle size increases, the differences between the two Tafel slopes fade down. For particles larger than 1 μm in size, a single Tafel slope is observed. Such changes in Tafel slope have been observed for various catalysts and are generally assigned to the increase of the surface coverage by hydrogen [31,32]. For electrodes showing larger surfaces, the HER starts at lower overpotentials. The limited values of Tafel slopes measured at low overpotential (LO) for the small particle based electrodes suggest the electrodesorption (Heyrowsky step (4)) as the limiting rate step. In contrast, the charge transfer at Volmer step (3) is very fast. For electrodes made of larger particles and for the Ni bulk electrode, high values of Tafel slopes are measured (at about 600 mV) at LO. These values are characteristic of an activation process of the electrode with insignificant gas evolution but definitively associated to HER faradic processes [33].

For small particles, from LO to HO, the observed change in the Tafel slope clearly indicates a change in the HER mechanism. At HO, larger Tafel slopes originate from large amounts of atomic and molecular hydrogen generated at the active surface. They are absorbed at the catalyst surface, eventually in the form of surface metal hydrides [34], and are suspected to moderate the hydrogen evolution. Here again, the increase in the Tafel slope is correlated to the size of the particles. The smaller the particles, the larger the increase in the Tafel slope from LO to HO: from 38 mV dec^{-1} (LO) to 220 mV dec^{-1} (HO) for 5 nm particles and from 102 mV dec^{-1} (LO) to 188 mV dec^{-1} (HO) for 27 nm particles. For particles larger than 1 μm in size, there is no change in the Tafel slope from LO to HO as the HER mechanism remains the same, i.e. a rate limited Volmer Heyrovsky mechanism.

For the entire electrode series, b_2 Tafel slopes at HO, range from 102 to 220 mV dec^{-1} pointing out the charge transfer reaction (Volmer Heyrovsky reaction) as the rate limiting step.

The overpotential values corresponding to a 100 mA cm^{-2} current density and exchange current densities are also reported in Table 2 as η_{100} and j_0 respectively. The former parameter is characteristic of the electrical energy required for a given production of hydrogen. Prepared electrodes are

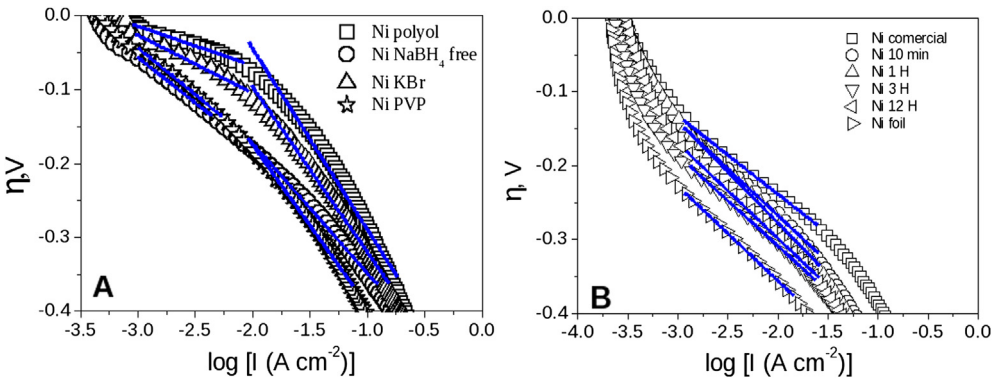

Fig. 8 – Tafel polarization curves for the HER on Ni nanoparticles obtained by chemical synthesis (A) and Ni particles obtained by mechanical synthesis (B). The scan rate was 1 mV/s at 20 °C.

Table 2 – Kinetics parameters from the polarization curves for the HER in 1 M KOH solution at 20 °C.

Catalyst	b_1 (mV dec $^{-1}$)	b_2 (mV dec $^{-1}$)	j_0 (mA cm $^{-2}$)	η_{100} (mV)
Chemically syntheses				
Ni polyol	38	221	0.497	286
Ni KBr	67	188	0.372	323
Ni PVP	102	188	0.342	410
Ni NaBH4 free	110	132	0.295	352
Mechanical syntheses				
Ni commercial		102	0.074	386
Ni 10 min		120	0.065	458
Ni 1 h		132	0.08	452
Ni 3 h		122	0.029	488
Ni 12 h		129	0.05	477
Ni foil		134	0.0217	522

characterized either by a higher exchange current density, j_0, and lower hydrogen overpotential, η_{100}, compared to the Ni foil electrode, thereby indicating an improved electrocatalytic activity.

Electrodes made of the smallest nickel particles with the higher strain prepared by the polyol route, simultaneously show the lowest hydrogen overpotential, η_{100} 286 mV, and the highest exchange current density, $j_0 \approx 0.5$ mA cm $^{-2}$.

Domingez Crespo et al. [21] reported Tafel slopes for HER on nickel nanoparticles, ranging from 138 and 172 mV dec $^{-1}$ (overpotentials lower than 100 mV were not considered for Tafel analysis by the authors). These values are in good agreement with those measured in the present study, although, in any case, present current exchange densities and η_{100} values demonstrate enhanced electrocatalytic performances. In the literature, catalytic performances (j_0 and η_{100}) of raw nickel electrodes, especially porous nickel electrodes [3,35–37], are comparable to those presented here despite a drastically lower Ni content in our electrodes. As an example, the Ni polyol based electrode exhibits an intrinsic activity of 2 A g $^{-1}$ at η 100 mV to compare with the 1 A g $^{-1}$ value reported for a porous electrode [38].

3.3.2. *Electrochemical impedance spectroscopy*

The electrochemical impedance spectroscopy (EIS) was used to further investigate the electrode/electrolyte interface characteristics and corresponding processes. EIS measurements were carried out at four different selected overpotentials. Fig. 9 shows EIS from the various chemically synthesized electrocatalysts (Ni polyol, Ni KBr, Ni PVP) as well as the commercial Ni powder. EIS spectra reveal the presence of two overlapped semicircles (corresponding to two different

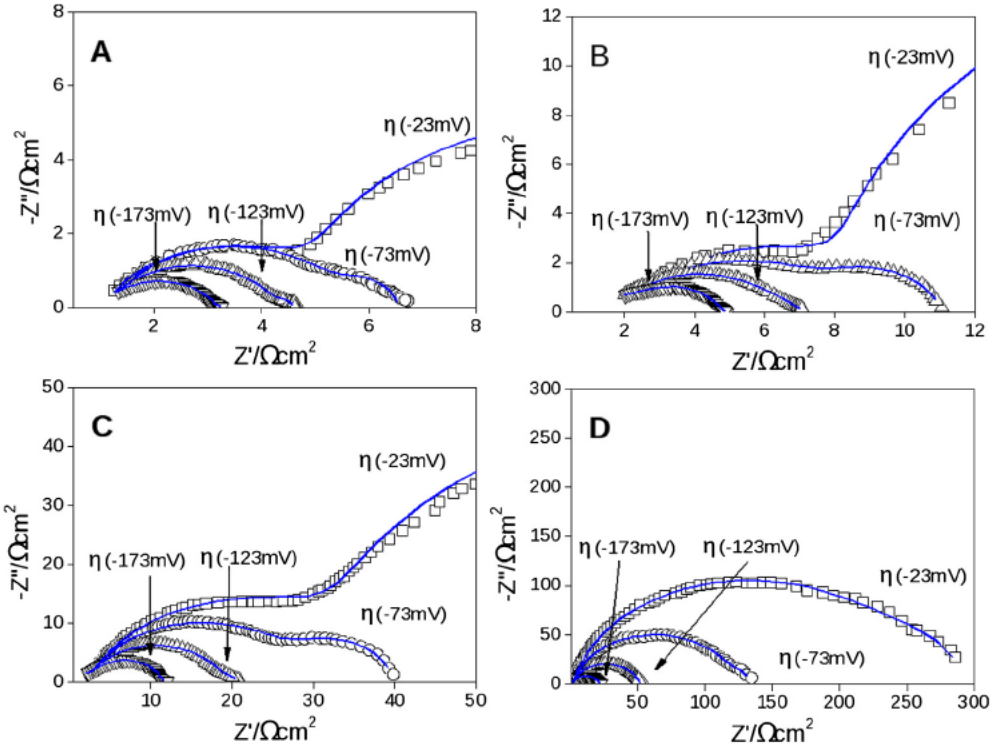

Fig. 9 – Complex plane plots for Ni polyol (A), Ni KBr (B), Ni PVP (C), commercial Ni (D) in 1 M KOH at 20 °C at four different overpotentials. Symbols are experimental data and continuous lines are data fitted by 1CPE model (Fig. 10A).

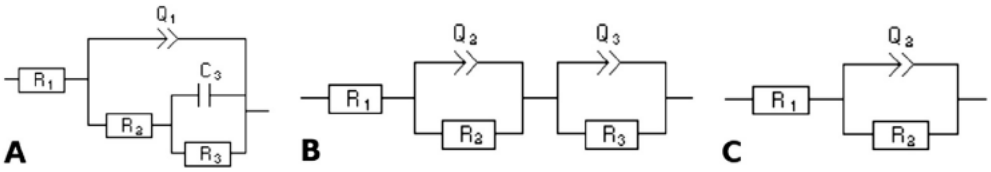

Fig. 10 – Equivalent circuits used for the HER. A. 1CPE model; B. 2CPE model, C. General model.

time constants), the first one at high frequencies (HF), and the second one at low frequencies (LF). As the overpotential is increased, the LF semicircle becomes smaller and even tends to disappear at HO.

To model EIS data, two electrical equivalent circuits were selected: the two time constant parallel (1 CPE) electric equivalent circuit (Fig. 10A), introduced by Armstrong and Henderson [39] and the two time constant series (2 CPE) electric equivalent circuit (Fig. 10B) proposed by Chen and Lasia [40]. The 1 CPE model expresses the faradic impedance of the HER as a combination of a charge transfer resistance, R_2, in series with an RC parallel circuit (R_3 and C_3). R_3 is the mass transfer resistance related to the intermediate (H_{ads}) adsorbed at the electrode surface and C_3 is a pseudo capacitance as it appears not from the electric double layer but from the Volmer Heyrovsky faradic reactions. Both semi circles are potential dependent. The first one is related to the charge transfer kinetics while the second one is related to the hydrogen adsorption. The 2 CPE model produces two semi circles in the complex plan plot, with the HF potential

Table 3 – Equivalent electrical circuit parameters of the 1CPE and 2CPE models obtained by fitting EIS experimental spectra recorded in 1 M KOH solution at various overpotentials and at 20 °C.

Model	Ni polyol								Ni KBr							
	5 nm average particle size								22 nm average particle size							
	1CPE				2CPE				1CPE				2CPE			
	η_1	η_2	η_3	η_4	η_1	η_2	η_3	η_4	η_1	η_2	η_3	η_4	η_1	η_2	η_3	η_4
η/mV	23	73	123	173	23	73	123	173	23	73	123	173	23	73	123	173
χ^2 ($\times 10^2$)	4.89	1.1	2.8	2.5	5.8	0.88	2.8	0.85	90	2.1	2.4	0.98	2.4	1.6	0.55	0.46
R_1/Ωcm^2	1.04	1.04	1.04	1.04	1.06	1.06	1.07	1.07	1.5	1.5	1.5	1.5	1.52	1.52	1.52	1.52
R_2/Ωcm^2	4.771	4.464	3.279	2.186	4.2	3.99	3.27	1.35	7.37	7.3	5.53	2.72	7.14	7.23	5.67	3.73
R_3/Ωcm^2	9.39	0.89	0.24	0.054	9.605	1.44			29.26	2.02	0.15	0.94	31.71	5.56		
Q1/mFs$^{(a\ 1)}$	31.22	24.7	22.58	19.12	29.87	23.6	22.54	18.36	24.12	24.18	20.5	10.51	25.03	23.49	21.74	17.86
Q2/mFs$^{(a\ 1)}$					446.3	876							248	163		
a_1	0.76	0.80	0.76	0.72	0.782	0.833	0.762	0.896	0.77	0.62	0.62	0.65	0.77	0.76	0.72	0.72
a_2					0.99	0.786							0.943	0.75		
C3/Fcm^{-2}	0.405	1.56	11.48	66.22	446.3	876			0.22	0.69	5.7 10^{-3}	0.013	248	163		
$C_{dl,1}$/mFcm^{-2}	10.2	10.16	6.5	3.8	10.7	10.7	6.45		8.5	3	2.2	0.96	8.9	7.72	5.15	4.26
$C_{dl,2}$/mFcm^{-2}					442.5								233.1	94.4		
Rf	510	508			22125				425	151			11657			

Model	Ni PVP								Commercial Ni							
	27 nm average particle size								1 μm average particle size							
	1CPE				2CPE				1CPE				2CPE			
	η_1	η_2	η_3	η_4	η_1	η_2	η_3	η_4	η_1	η_2	η_3	η_4	η_1	η_2	η_3	η_4
η/mV	23	73	123	173	23	73	123	173	23	73	123	173	23	73	123	173
χ^2 ($\times 10^2$)	3.6	6.5	4.4	7.5	2.9	6.7	4.4	1.3	4.3	4.2	3	1.4	2.2	1.9	5.2	2.1
R_1/Ωcm^2	2	2	2	2	2.2	2.2	2.2	2.2	1.95	1.95	1.95	1.95	1.78	1.78	1.78	1.78
R_2/Ωcm^2	38.8	28.1	17.45	10.4	30.88	26.94	17.39	7.36	257.5	121.7	5.75	6.54	131.1	95.3	48.77	16.9
R_3/Ωcm^2	82.2	9.5			94.42	10.54			33.92	10.73			168.2	43		
Q1/mFs$^{(a\ 1)}$	8.2	6.5	5.3	4.4	8.06	6.55	5.3	4.2	2.5	2.2	1.9	1.78	3.37	2.26	2.07	1.82
Q2/mFs$^{(a\ 1)}$					93	271							8.7	2.9		
a_1	0.786	0.787	0.784	0.75	0.81	0.79	0.78	0.89	0.87	0.873	0.8253	0.831	0.96	0.93	0.87	0.9
a_2					0.94	0.99							0.735	0.58		
C3/Fcm^{-2}	0.093	0.263			93	271			0.136	0.39			8.7	2.9		
$C_{dl,1}$/mFcm^{-2}	2.56	2	1.5	0.86	3.1	2.06	1.15		1,13	1	0.53	0.52	2.74	1.5		
$C_{dl,2}$/mFcm^{-2}					84.6								1.95			
Rf	132	100			4232				57	50			97.2			

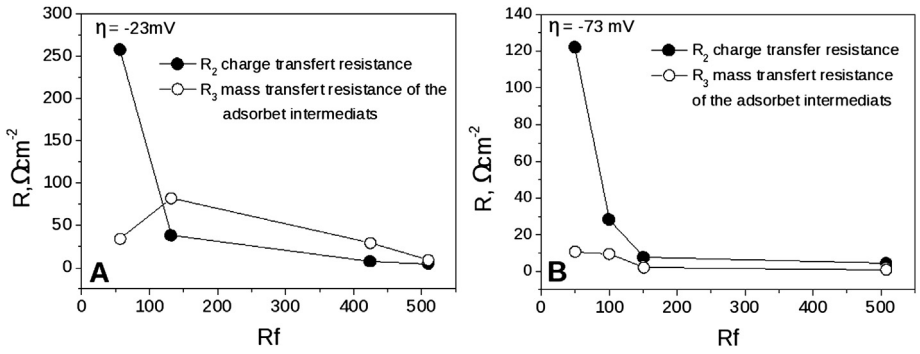

Fig. 11 – Evolution of charge transfer resistance and mass transfer resistance with surface roughness at $\eta = -23$ mV(A) and at $\eta = -73$ mV(B).

independent semicircle related to the surface porosity, and the LF potential dependent semicircle related to the charge transfer process. For this model, the R_2 resistance is assigned to the electrolyte resistance in the electrode porosity and is independent of the kinetics of the faradic process. The R_3 resistance is related to the kinetics of the faradic reaction of the HER. For the highest overpotentials values, a single semicircle is observed and a general model is used to fit the experimental data (Fig. 10C).

The double layer capacitance was approximated by a constant phase element (CPE) to account for the non ideal behaviour of the capacitive elements due to surface hetero geneities including surface roughness, impurities, disloca tions and grain boundaries [41].

The average double layer capacitances, C_{dl}, for the elec trodes were calculated using the relation suggested by Brug et al. [42] (equation (6)).

$$C_{dl} \quad \left[Q_i/\left(R_1^{\ 1} + R_{i+1}^{\ 1}\right)^{(1\ a_{i+1})}\right]^{(1/a_{i+1})} \qquad (6)$$

with i 1 or for 1CPE and 2CPE respectively

where Q_i and a_{i+1} are the CPEi (with i 1 or 2) constant and exponent, respectively. R_1 is the solution resistance and R_{i+1} the HER charge transfer resistance. Considering a value of 20 μF cm ^{2} for the double layer capacitance of a smooth nickel surface, used earlier in the literature [43], the real active sur face area, in terms of surface roughness factor (Rf), may be estimated by comparing the C_{dl} related to the charge transfer kinetics of porous/rough and smooth electrodes.

Table 3 shows the best fit estimates of the equivalent electrical circuit parameters obtained from the impedance measurements of prepared electrodes, by using the selected models. The fit accuracy from calculated parameters (expressed by Chi squared value) are close from one to the other model making, at first, difficult the choice for the model to select.

The variation of the HF semicircle radius with the over potential depends on the size of the particles. For the elec trodes made of the smallest particles (Ni polyol, and Ni KBr) this variation is rather weak especially for the lowest over potentials, η 23 mV and η 73 mV. For the electrodes made of larger particles (Ni PVP and Ni commercial), the HF semicircle clearly decreases as the overpotential is increased. Thanks to this decrease, the HF semicircle can be assigned to the change transfer kinetics, as suggested by the 1CPE model. In contrast, C_3 increases as the overpotential increases while R_3 rapidly drops down. This behaviour is typically associated to the adsorption of hydrogen at the electrode surface and the LF semicircle can then be assigned to this phenomenon. Sur face roughnesses, Rf, were calculated using equation (6). Since they are directly correlated, either Rf and particle sizes will be used for EIS analysis.

Using this 1CPE model, some correlations can be drawn between the characteristics of the Tafel plots (changes in slope)

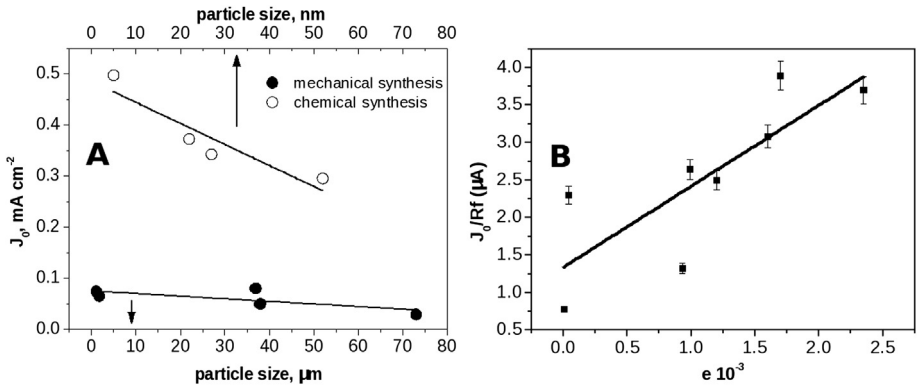

Fig. 12 – Evolution of the current exchange density with particle sizes (A) and of the intrinsic catalytic activity with strain (B).

Table 4 – Exchange current densities corrected with the surface roughness factor obtained from the polarisation curves in 1 M KOH at 20 °C. Rf values are calculated by EIS technique.

Catalyst	Ni polyol	Ni KBr	Ni PVP	Ni $NaBH_4$ free	Ni non milled	Ni 10 min	Ni 1H	Ni 3H	Ni 12H
Rf	510	425	132	128	57	28	24	19	20
j_0/Rf, μA cm ^{2}	0.98	0.78	2.5	2.3	1.32	2.64	3.08	3.9	3.7

and the relative magnitude of the semicircles. The latter can be interpreted as a proof of changes in the reaction mechanism. In addition to the overpotential applied, the charge transfer resistance R_2 and the R_3 resistance related to the mass transfer of the adsorbed intermediates at the electrode surface depend on the particle size too. Fig. 11 shows the resistances R_2 and R_3 as a function of the particles size at η 23 mV and η 73 mV. At the lowest overpotential, η 23 mV (Fig. 11A), for the electrodes made of particles ranging from 5 to 27 nm in size, as R_3 is larger than R_2, the process kinetics are limited by the adsorbed hydrogen at the surfaces (Heyrowsky step (4)). In contrast, for electrodes made of micro sized particles, the charge transfer resistance R_2 is larger than R_3 and the process is limited by the charge transfer reaction (Volmer step (3)). At HO, i.e η 73 mV, the charge transfer resistance controls the process independently on the particle size (Fig. 11B) since R_2 is larger than R_3 in the whole series. For overpotentials greater than 73 mV, both charge transfer and electrodesorption processes cannot be distinguished as corresponding semi circles are merged. The above description is in good agreement with the above Tafel plot analysis.

As shown in Fig. 8A, η 73 mV appears as a critical overpotential, marking a drastic change in the kinetics mechanism and limiting step. Below this limit, the charge transfer is very fast and the corresponding R_2 resistance re mains low. Because of this limited changes in the HF semi circle radii (and correlatively in R2 values), the 2CPE model can be used for comparison to the 1CPE kinetics model. In this 2 CPE model, the HF semicircles are related to the electrode porosity and corresponding R_2 resistances are expected not to depend on the overpotential. Calculated parameters are re ported in Table 3.

However, some parameters extracted from the 2CPE model suffer from inconsistencies as demonstrated as follows. From LF semicircle, roughness factors were calculated by using the charge transfer resistances R_3. Rf values from the 2CPE model (Table 3) are larger than those extracted from the 1CPE model (Table 3). This observation was already done by Kelenberger et al. [44] and assigned to the different physical meanings of the two models. R_F is the ratio between the electrode active surface and the electrode geometrical surface. The theoretical surface of spherical nickel nanoparticles with an average size of 5 nm is about 60 m^2 g^{-1}. Calculated surface from Rf using the 2CPE model for the corresponding 5 nm polyol Ni nano particles is about 442 m^2 g^{-1} which is by far overestimated.

Based on this critical analysis of HF and LF semicircles assignments, the 1CPE model is obviously more suited to model these EIS data suggesting the HF semicircles to be more likely related to the kinetics of the HER than to the porosity of the electrode.

Another critical kinetics parameter for HER is j_0 as it pro vides information about the intrinsic catalytic activity of the electrode material. To uncorrelate the geometric and elec tronic effects, values of j_0 and Rf are discussed in the following section. Fig. 12A shows j_0 as a function of the particle size determined by SEM or TEM in each case. These data cannot fit all together because of a scale change (from nm to μm) but in each series of prepared electrode materials, the smaller the particles the higher j_0 and, correlatively, the greater the apparent electrochemical activity.

By eluding the contribution of the surface area, Rf allows the evaluation of the relative intrinsic catalytic activity of the investigated catalysts. Rf extracted from EIS data (Fig. 9 and Table 3, and Figure SI 4 and Table SI 1) and j_0/Rf ratio are collected in Table 4. There are drastic discrepancies in the j_0/Rf ratio in the series which are characteristic of great differences in electrochemical activities of the prepared electrode mate rials despite the unique Ni composition. As expected, the smaller the particles the larger j_0/Rf ratio. Moreover, ratios are greater for milled powders than for synthesised nanoparticles.

A general assertion found in the literature [45] is that the intrinsic catalytic activity for the HER is related to the elec tronic structure of the metal surface. On the other hand, strain appears as a good marker for material electronic structure as it characterizes the defects in the local environment of Ni atoms. This is clearly confirmed by the linear evolution of intrinsic catalytic activity with strain as shown in Fig. 11B. Particles with the larger structure strain, i.e. the larger numbers of defects with electronic structure discrepancies present the better intrinsic catalytic activity.

4. Conclusion

A versatile route was used for the chemical synthesis of nickel nanoparticles in aqueous medium. By using various stabiliz ing agents, nickel particles with various morphologies, sizes and strains were obtained. For comparison a polyol route was used too.

In a different approach, micro sized Ni catalytic powders were obtained by mechanical milling of a commercial nickel powder.

The catalytic performance on HER was evaluated for each prepared nickel catalyst. Tentative to draw a trend between size and morphology descriptors of nickel particles and ki netics parameters for HER was successful. A monotone trend between material strain and intrinsic activity was experi mentally observed. The HER reaction on various nickel mor phologies is dominated by the surface roughness of the electrode. Ideally, and in terms of catalytic activity, electrodes made of small particles with high internal strain are expected to show serious performance advantages compared to larger unstrained particles.

The catalytic activity of the prepared Ni particles was studied only for short time measurements and further tests must be done to assess on their long term stability.

Acknowledgements

A.P. Would like to acknowledge the BULANE Company and CNRS for PhD fellowship and funding.

Appendix A. Supplementary data

Supplementary data related to this article can be found at http://dx.doi.org/10.1016/j.ijhydene.2013.06.045.

REFERENCES

[1] Zeng K, Zhang D. Recent progress in alkaline water electrolysis for hydrogen production and applications. Prog Energy Combust 2010;36:307 26.
[2] Mueller Langer F, Tzimas E, Kaltschmitt M, Peteves S. Techno economic assessment of hydrogen production processes for the hydrogen economy for the short and medium term. Int J Hydrogen Energy 2007;32(6):3797 810.
[3] Hitz C, Lasia A. Experimental study and modelling of impedance of the her on porous Ni electrodes. J Electroanal Chem 2001;500(1 2):213 22.
[4] Los P, Rami A, Lasia A. Hydrogen evolution reaction on Ni Al electrodes. J Appl Electrochem 1993;23(2):135 40.
[5] Chen LL, Lasia A. Study of the kinetics of hydrogen evolution reaction on nickel zinc alloy electrodes. J Electrochem Soc 1991;138(11):3321 8.
[6] Kellenberger A, Vaszilcsin N, Brandl W, Duteanu N. Kinetics of hydrogen evolution reaction on skeleton nickel and nickel titanium electrodes obtained by thermal arc spraying technique. Int J Hydrogen Energy 2007;32(15):3258 65.
[7] Burchardt T. Hydrogen evolution on NiPx alloys: the influence of sorbet hydrogen. Int J Hydrogen Energy 2001;26(11):1193 8.
[8] Shervedani RK, Lasia A. Studyes of the hydrogen evolution reaction on Ni P electrodes. J Electrochem Soc 1997;144(2):511 9.
[9] Huang YJ, Lai CH, Wu PW, Chen LY. Ni inverse opals for water electrolysis in an alkaline electrolyte. J Electrochem Soc 2010;157(3):18 22.
[10] Herraiz Cardona I, Ortega E, Vazquez Gomez L, Perez Herranz V. Electrochemical characterization NiCo/Zn cathode for hydrogen generation. Int J Hydrogen Energy 2011;36(18):11578 87.
[11] Solmaz R, Kardas G. Fabrication and characterization of NiCoZn M (M: Ag, Pd and Pt) electrocatalysts as cathode materials for electrochemical hydrogen production. Int J Hydrogen Energy 2011;36(19):12079 87.
[12] Han Q, Cui S, Pu N, Chen J, Liu K, Wei X. A study on pulse plating amorphous Ni Mo alloy coating used as HER cathode in alkaline medium. Int J Hydrogen Energy 2010;35(11):5194 201.
[13] Rodriguez Valdez LM, Estarda Guel I, Almeraya Calderon F, Neri Flores MA, Martinez Villafane A, Martinez Sanchez R. Electrochemical performance of hydrogen evolution reaction of Ni Mo electrodes obtained by mechanical alloying. Int J Hydrogen Energy 2004;29(11):1141 5.
[14] Kedzierazawski P, Oleszak D, Janik Czachor M. Hydrogen evolution on hot and cold consolidated Ni Mo alloys produced by mechanical alloying. Mater Sci Eng A 2001;300(1 2):105 12.
[15] Shervedani RK, Lasia A. Study of the hydrogen evolution reaction on Ni Mo P electrodes in alkaline solutions. J Electrochem Soc 1998;145(7):2219 25.
[16] Krstajic NV, Gajic Krstajic LJ, Lacnjevac U, Jovic BM, Mora S, Jovic VD. Non noble metal composite cathodes for hydrogen evolution. Part I: the Ni MoO_x coatings electrodeposited from Watt's type baths containing MoO3 powder particles. Int J Hydrogen Energy 2011;36(11):6441 9.
[17] Solmaz R, Kardas G. Electrochemical deposition and characterization of NiFe coatings as electrocatalytic materials for alkaline water electrolysis. Electrochim Acta 2009;54(14):3726 34.
[18] Danaee I, Noori S. Kinetics of the hydrogen evolution reaction on NiMo graphite modified electrode. Int J Hydrogen Energy 2011;36(19):12102 11.
[19] Solmaz R, Doner A, Kardas G. Electrochemical deposition and characteisation of NiCu coatings as cathode materials for hydrogen evolution reaction. Electrochem Commun 2008;10:1909 11.
[20] Dominguez Crespo MA, Torres Huerta AM, Brachetti Sibaja B, Flores Vela A. Electrochemical performance of Ni RE (RE = rare earth) as electrode material for hydrogen evolution reaction in alkaline medium. Int J Hydrogen Energy 2011;36(1):135 51.
[21] Dominguez Crespo MA, Ramirez Meneses E, Montiel Palma V, Torres Huerta AM, Dorantes Rosales H. Synthesis and electrochemical characterization of stabilyzed nickel nanoparticles. Int J Hydrogen Energy 2009;34(4):1664 76.
[22] Domingues Crespo MA, Ramirez Meneses E, Torres Huerta AM, Garibay Febles V, Philippot K. Kinetics of hydrogen evolution reaction on stabilized Ni, Pt and Ni Pt nanoparticles obtained by an organometalic approch. Int J Hydrogen Energy 2012;37(6):4798 811.
[23] Chen PC, Chang YM, Wu PW, Chiu YF. Fabrication of Ni nanowiers for hydrogen evolution reaction in a neutral electrolyte. Int J Hydrogen Energy 2009;34(16):6596 602.
[24] Couto G, Klein JJ, Schreiner WH, Mosca DH, de Oliviera AJA, Zarbin AJG. Nickel nanoparticles obtained by a modify polyol process: synthesis, characterization and magnetic proprieties. J Colloid Inter Sci 2007;311(2):461 8.
[25] Jerkiewicz G. Hydrogen sorption at/in electrodes. Prog Surf Sci 1998;57(2):137 86.
[26] Zhang DL. Processing of advanced materials using high energy mechanical milling. Prog Mater Sci 2004;49(3 4):537 60.
[27] Zhao X, Ding Y, Ma L, Shen X, Xu S. Structure, morphology and electrocatalytic characteristics of nickel powder treated by mechanical milling. Int J Hydrogen Energy 2008;33(21):6351 6.
[28] Wolf JF, Yeh LS, Damjanovic A. Anodic oxide films at nickel electrodes in alkaline solutions. 1. Kinetics of growth of the beta $Ni(OH)_2$ phase. Electrochim Acta 1981;26(3):409 16.
[29] Lyons MEG, Brandon MP. The oxygen evolution reaction on passive oxide covered transition metal electrodes in aqueous alkaline solutions. Part 1 Nickel. Int J Electrochemical Sci 2008;3(12):1386 424.
[30] Bode H, Dehmelt K, Witte J. Zur kenntnis der nickelhydroxidelektrode I. Über das nickel (II) hydroxidhydrat. Electrochim Acta 1966;11(8):1079 87.
[31] Ohmori T, Go H, Nakayama A, Mametsuka H, Suzuki E. Influence of spittering parameters on hydrogen evolution overvoltage in sputter deposited Co Mo alloy electrode. Mater Lett 2001;47:103 6.
[32] Simpraga R, Tremiliosi Filho G, Qian SY, Conway BE. In situ determination of the 'real area factor' in H_2 evolution

electrocatalysis at porous Ni Fe composite electrodes. J Electroanal Chem 1997;424(1 2):141 51.
[33] Krstajic N, Popovic M, Grgur B, Vojnovic M, Sepa D. On the kinetics of the hydrogen evolution reaction on nickel in alkaline solution: Part1: the mechanism. J Electroanal Chem 2001;512(1 2):16 26.
[34] Varcar L, Conway BE. Hydride formation at Ni coating glassy metal electrodes during the H_2 evolution reaction in alkaline solutions. J Electroanal Chem 1990;277(1 2):253 75.
[35] Brown IJ, Sotiropoulos S. Preparation and characterization of microporous Ni coatings as hydrogen involving cathodes. J Appl Electrochem 2000;30(1):107 11.
[36] Rausch S, Wendt H. Morphology and utilization of smooth hydrogen evolving raney nickel cathode coatings and porous sintered nickel cathodes. J Electrochem Soc 1996;143(9):2852 62.
[37] Herraiz Cardona I, Ortega E, Vazquez Gomez L, Perez Herranz V. Double template fabrication of three dimensional porous nickel electrodes for hydrogen evolution reaction. Int J Hydrogen Energy 2012;37(3):2147 56.
[38] Ganesh V, Lakshminarayanan V. Preparation of high surface area nickel electrodeposit using a liquid crystal template technique. Electrochim Acta 2004;49(21):3561 72.
[39] Armstrong RD, Henderson M. Impedance plan display of a reaction with an adsorbed intermediate. J Electroanal Chem 1972;39(1):81 90.
[40] Chen LL, Lasia A. Hydrogen evolution reaction on nickel molybdenum powder electrodes. J Electrochem Soc 1992;139(12):3258 64.
[41] Boresen B, Hagen G, Tunold R. Hydrogen evolution on $Ru_xTi_{1-x}O_2$ in 0.5 M H_2SO_4. Electrochim Acta 2002;47(11):1819 27.
[42] Brug GJ, Vandeneeden ALG, Sluytersrehbach M, Sluyters JH. The analysis of electrode impedance complicated by the presence of a phase constant element. J Electroanal Chem 1984;176(1 2):275 95.
[43] Rami A, Lasia A. Kinetics of hydrogen evolution on Ni Al alloy electrodes. J Appl Electrochem 1992;22(4):376 82.
[44] Kellenberger A, Vaszilcsin N, Brandl W. Roughness factor evaluation of thermal arc sprayed skeleton nickel electrodes. J Solid State Electrochem 2007;11(1):84 9.
[45] Herraiz Cardona I, Ortega E, Garcia Anton J, Perez Herranz V. Assessment of roughness factor effect and the intrinsic catalytic activity for hydrogen evolution reaction on Ni based electrodeposits. Int J Hydrogen Energy 2011;36(16):9428 38.